Graphene Thickness-controlled Photocatalysis and Surface enhanced Raman Scattering

Cheng-Chi Kuo and Chun-Hu Chen*

Department of Chemistry, National Sun Yat-sen University, Kaohsiung, Taiwan 80424

Abstract

Exceptional photocatalytic enhancement of graphene-semiconductor composites has been widely reported, but our understanding of the role that graphene plays in this enhancement remains limited, which arise from the difficulty of precisely controlling graphene hybridization. Here we present a general platform of graphene-semiconductor hybrid panel (GHP) system wherein a precise number of layers of graphene are hybridized with photoactive semiconductors (e.g. TiO_2, ZnO) to study systematically how graphene affects the photocatalysis. The results show that the graphene enhancement of the photocatalysis depends on the number of graphene layers, with the maximum performance observed at 3 layers. Photodeposited indicators of gold particles further reveal that graphene thickness governs the density of photocatalytic sites and charge transfer efficiency at the graphene/semiconductor interfaces. We suggest that quantized energy levels caused by different numbers of graphene sheet stacking along the vector normal to graphene basal plan affect the charge transfer routes and lead to the graphene thickness-controlled photocatalysis. GHP substrates deposited with gold particles are promising, uniform substrates for surface enhanced Raman scattering (SERS) applications with the enhancement factor as high as $\sim 10^8$ on 3-layer graphene.

Key words: graphene, photodegradation, SERS, titania, thickness

1. Introduction

Graphene-semiconductor hybrid composites, which take advantage of superior optical, mechanical, and electrical properties of graphene,[1-3] have enabled impressive enhancement in the performance of batteries, solar cells, sensors, catalysis, and environmental protections.[4-10] Although extensive effort has been concentrated on exploiting the exceptional activities observed in these composites, the mechanisms and principles that result in graphene-enhanced performance remain unclear. As graphene is a basal-plane quantized form of bulk graphite, the origin of graphene-enhanced properties is expected to depend highly on the number of graphene layers.[11, 12] Yet, systematic studies of the correlation between graphene thickness at the hybridizing interfaces and the enhancement of properties is largely lacking.

Photocatalysis is critical for water splitting, CO_2 activation, and pollutant degradation.[13-16] The colloidal graphene hybrid nanocomposites comprised of reduced graphene oxide (rGO) and photoactive semiconductors (e.g. TiO_2, ZnO) are well recognized for their highly enhanced photocatalysis,[17-25] but dependence of their photocatalytic performance on graphene thickness has not been described. The major challenge to study the effect of graphene thickness comes from uncontrollable assembly/stacking of colloidal graphene sheets during the typical preparation of graphene/semiconductor hybrids.[17, 26] The difficulty of directly measuring a property of interest (e.g. conductivity, coverage, transparency, surface energy, etc.) in colloids further impedes the discovery of the factors that govern the performance of graphene-enhanced photocatalysis. To enable systematic studies of how graphene-enhanced photocatalysis is affected by graphene thickness, we developed a general platform of graphene-semiconductor hybrid panels (GHPs) with well-controlled graphene size, coverage, and thickness at the graphene/semiconductor interfaces (Fig. 1). Such the hybrid interfaces with the presence of TiO_2 can be considered as graphene/TiO_2 hybrid composites to simulate the colloidal these reported in the literature.[4, 19-21] The solid, flat panel supports of GHPs enables the measurement of conductivity, surface energy, transparency, and other properties. This GHP system is also free of the uncertainties of surface area, graphene/semiconductor ratios, and aggregation that plague the reported colloidal composites.

In this study, we reveal that graphene-enhanced photocatalysis is directly controlled by the number of the stacked graphene sheets at the graphene/semiconductor interface. Three-layer (3L) graphene represents the optimal photocatalytic performance, both for pristine and oxygen-modified graphene. We implemented the strategy of photoelectron scavenger addition to visually indentify the locations and densities of interfacial photocatalytic sites by photodeposition of gold particles, and thereby to

confirm the dependence of the photocatalytic efficiency on graphene thickness. Quantized energy levels varied with the number of graphene sheet stacking play a critical role in graphene thickness-controlled photocatalysis. The high coverage density of gold particles on 3L graphene results in a uniform distribution of hot spots, highly promising for applications of surface enhanced Raman scattering (SERS). The results of this work show that controlling graphene thickness would produce graphene hybrid composites with unprecedented performance.

2. Results

2.1.   GHP fabrication

Continuous and single-layer graphene (SLG) on a centimeter scale was produced on copper foils by the chemical vapor deposition (CVD) method.[27] The SLG was then transferred to the top of photoactive semiconductor/quartz substrates with the desired phases (Fig. S-1). By repeating the SLG transfer process, an arbitrary number of graphene sheets in GHPs can be deposited by layer-by-layer assembly. The demonstration of layer-by-layer assembly of graphene (Fig. S-2) visibly on 300 nm SiO_2/Si showed that graphene stacking with controlled coverage area, sizes, shapes, and thickness can be precisely achieved. A series of GHPs was fabricated with one, three, five, and seven layer graphene sheets on TiO_2/quartz substrates, denoted as **1L-GHP**, **3L-GHP**, **5L-GHP**, and **7L-GHP**, respectively (Fig. 1). The layer-by-layer stacking of individual graphene sheets simulated more closely the hybridizing situations of colloidal graphene nanocomposites than does the direct production of multi-layer graphene materials.[19] The photographs of GHPs showed that the darker contrast of graphene area is observed with the greater numbers of SLG stacks (Fig. 1b). For **1L-GHP**, the characteristic 2D band (~ 2690 cm^{-1}) observed in the Raman spectrum was highly symmetrical with a full width at half-maximum (FWHM) of ~ 32 cm^{-1}, and the intensity of ~ 2.6 times that of the G band (~ 1595 cm^{-1}), consistent with the presence of SLG (Fig. 2a).[28, 29] The negligible D band at ~ 1345 cm^{-1} showed the high quality of CVD graphene with low defect content. We further conducted the characterization of transmission electron microscopy (TEM) and atomic force microscopy (AFM) to verify the formation of single-layer graphene. The AFM results of the CVD graphene transferred onto a 300 nm SiO_2/Si wafer exhibited a thickness of 0.8 nm (Fig. S-3a), corresponding to that of monolayer graphene in the literature.[30, 31] The TEM images showed the presence of SLG cross section (Fig. S-3b).[31] The corresponding selected area electron diffraction (SAED) pattern illustrated the hexagonal arrays of diffraction spots of equivalent {1100} and {2110} plans, indicating the presence of SLG (Fig. S-3c).[27] Different from bi-layer graphene in the literature,[32] the single set of hexagonal array of diffraction spots suggested no

3

presence of additional layers of graphene with various orientations. These results confirm the use of SLG as the graphene stacking unit to construct GHPs. The Raman spectra of 1L to 7L graphene showed the typical trend of intensity variation of 2D/G ratios and the small red shift of 2D bands, consistent with the increase of graphene layers observed in the literature.[27, 29]

2.2. Graphene thickness-dependent photocatalysis

The photocatalytic activities of GHPs with different numbers of stacked graphene sheets were evaluated via the photodegradation of organic dyes (methylene blue, MB) under the UV irradiation in aqueous solutions. The incident UV light came from all directions onto vertically standing GHPs due to the highly-reflective cylindrical mirror in our photoreactor (Fig. 1a and S-4). The time profile of MB degradation was determined by monitoring the changes of MB concentrations (C/C_0) derived from the evolution of characteristic absorbance (A/A_0) of MB at 665 nm, where C_0 and A_0 are the initial concentrations and the corresponding absorbance values of the MB solutions, respectively.[20] The bare TiO_2 panels exhibited certain photocatalytic activities toward dye decomposition (Fig. 3). The photodegradation rate constant of **1L-GHP** was twice that of the bare TiO_2 panels, confirming the formation of effective graphene-photocatalyst hybridization interfaces. The presence of graphene clearly enhanced the degradation efficiency of GHPs (Fig. 3). Among the GHPs studied, **3L-GHP** showed the highest photodecomposition activity with the degradation rate constant of 2.01×10^{-3} min^{-1}, which was around 5 times greater than the bare TiO_2 panels. The cycle tests of photodegradation of **3L-GHP** demonstrated the highly stable activities after five cycles (Fig. 3c). In contrast, **7L-GHP** shows a very limited photocatalytic enhancement (~30% increase) compared to the bare TiO_2. The order of photodegradation rate constants was: **3L-GHP** > **5L-GHP** > **1L-GHP** > **7L-GHP** > TiO_2.

Specific adsorption of molecules to the catalyst surface commonly affects the catalytic efficiency and selectivity. Selective photodegradation of MB dyes caused by their easy absorption on graphene-semiconductor photocatalysts, possibly due to similar chemical structures and π-π interaction between MB molecules and graphene surface, is recognized.[33, 34] To test that the order of the activity in the series of GHPs was not due to specific absorption, we measured the kinetics of photodegradation of an aromatic-ring-free polymer dyes, polydiacetylenes (PDA),[35, 36] and found the order to be similar to that of MB dyes with **3L-GHP** manifesting the fastest degradation (Fig. S-5). This result suggested that the order of photocatalytic efficiency of GHPs could be general for diverse substrates.

2.3. Effects of surface energy and transparency on photocatalysis

It is intriguing that graphene-enhanced performance is generally related to graphene thickness, as the trend described in the previous section shows. To understand this trend we studied the effects of surface energy and transparency, both showing correlation with graphene thickness (Fig. 1). The comparison of these parameters between **3L-GHP** and **7L-GHP** is particularly informative due to the greatest difference between their photodegradation activities.

Figure 1 shows that the contact angles of GHPs increase with the number of SLG sheets, plateauing at **5L-GHP** (also Table 1). The contact angle difference between **3L-GHP** and **7L-GHP** is quite small (5.3%), despite the large difference of their photodegradation rate constants (~330%). To further clarify the surface energy effect, we oxidized the graphene surface of **1L-GHP**, **3L-GHP**, and **7L-GHP** with oxygen plasma to increase surface hydrophilicity for aqueous photodegradation. The resulting samples were denoted **O-1L-GHP**, **O-3L-GHP**, and **O-7L-GHP**. As shown in Table 1, the decrease of both water contact angles and electric conductivities for these three samples confirmed the surface modification with oxygen. The Raman spectra of **O-1L-GHP** showed the dramatic increase of the D band with the much weaker intensity of the 2D peak relative to the G band, characteristic of the typical GO Raman spectra.[37] **O-3L-GHP** displayed the increase of D band but there was no significant change of the 2D/G ratios. Raman spectra of **7-GHP and O-7-GHP** were very similar to each other. These results suggested that only the top graphene layer was oxidized while the inner layers remained intact (Fig. 2b).

Photocatalytic activities of plasma-oxidized GHPs were generally higher than the pristine samples (Fig. 4a and S-6), showing that hydrophilic surface facilitated the aqueous photocatalysis. The largest increase of rate constant (~80%) was observed for **O-3L-GHP**, while **O-1L-GHP** and **O-7L-GHP** manifested improvements below 30%, illustrating again the critical role of graphene thickness in photocatalysis, particularly for 3L graphene.

Thicker graphene stacks exhibited darker contrast than thinner ones (Fig. 1). The transmittance measurement (Fig. 4b) showed that all the GHPs partially transmit UV light at 365 nm, the wavelength used for all the photocatalysis testes in this work. As GHPs were irradiated by UV light at all directions, the lower transparency of thicker graphene stacks (e.g., 7L graphene, transmittance ~40%) may block a portion of UV light and limit the photodegradation performance. To study the transparency effect, original **3L-GHP**s were modified by depositing four SLGs on the back side to obtain new panels, **3L-GHP-4L**, exhibiting similar transmittance to **7L-GHP**. Yet we measured the same photodegradation activity for **3L-GHP-4L** and **3L-GHP** (Fig. 4a), despite their different UV-light transmittance. Thus the possibility that lower

photodegradation activity of 5L and 7L GHPs results from smaller fraction of incident light reaching the interface is unlikely, and **7L-GHP** possesses the intrinsically lowest activity in the series. In the optical absorption results (Fig. S-7), similar absorbance of **7L-GHP** and **3L-GHP-4L** greater than that of **3L-GHP** at 365 nm was observed, suggesting no systematic correlation between the absorption activity of GHPs and their photocatalytic performance.

2.4. Labelling of charge transfer sites at the hybrid interfaces

Photodegradation is highly related to the efficiency of charge transfer and migration processes. Typical photocatalytic mechanism of TiO_2 under UV light irradiation is shown in Fig. S-8.[13, 20, 21, 38] Different from the photocatalytic mechansim under visible-light irradiation,[39-41] the TiO_2 layer absorbes the UV-light energy leading to the charge separation inside TiO_2. After UV light excitation, the generated photoelectrons at TiO_2 conduction band (CB) are transferred to molecular oxygen to yield reactive oxygen species for photodecomposition. The holes in valence band (VB) would oxidize water molecules to form highly oxidative radicals for decomposition as well. To investigate the dependence of graphene thickness on photocatalysis at the hybrid interface, we introduced Au^{3+} ions as a photoelectron scavenger, whose reduction generated nanoparticles at charge-transfer sites, to visually locate, and to compare the density of, the photocatalytic sites (Fig. S-8).

We used SEM to quantify the distribution and localization of nanoparticles (Fig. 5). The particle coverage densities in **3L-GHP** were substantially higher than in **1L-GHP** and **7L-GHP**, corresponding to a higher density of the charge-transfer sites and hence larger flux of reactive oxygen species for photodecomposition. The coverage densities correlated well with the trend of photodegradation activities (Fig. 3), thus validating the efficacy of monitoring photocatalytic sites through gold-particle indicators. The surface coverage of **O-3L-GHP** (Fig. 5d) exceeded that of **3L-GHP**, showing a good agreement with photocatalytic enhancement caused by surface oxygen plasma treatment. With the solid and flat support of GHPs, this is the first time that the distribution of photocatalytic charge-transfer sites on a graphene surface can be visualized. These results confirm that the improvement in charge-transfer efficiency and photoelectron flux with the number of the stacked graphene sheets is directly responsible for the enhanced photocatalytic activities of GHPs.

2.5. Gold-deposited GHP for SERS applications

Graphene and gold are two of the most promising materials in SERS applications for label-free, high-sensitive detection of specific biomedical targets, such as viruses and DNA.[42-45] In SERS technique, the locations with a strong near field enhancement

due to the surface plasmon resonance of gold particles, the so-called hot spots, are closely related to the distribution density and inter-particle spacing of gold nanoparticles.[46] Together with TiO_2 semiconductor, the gold-deposited GHPs with continuous, homogeneous graphene membrane and high coverage density of gold particles are promising candidates as highly uniform, sensitive SERS substrates.[47]

The SERS spectra of Rhodamine 6G (R6G) on different gold-deposited GHP substrates under a 633 cm^{-1} laser are shown in Fig. 6. The Raman peaks labelled with stars corresponded well to the vibration modes of R6G.[42] The SERS signals of R6G on gold-deposited **3L-GHP** were much stronger, indicating more uniform distribution of hot spots than that of gold-deposited **7L-GHP** and **1L-GHP** (Fig. 6a). We measured the SERS enhancement factor (EF) for gold-deposited **3L-GHP** of ~10^8, better or comparable to EFs of much finer gold nanoparticles and graphene-related substrates in the literature.[48, 49] In Fig. 6b, the EF order of gold-deposited **3L-GHP** > **1L-GHP** > **7L-GHP** > TiO_2 was observed, demonstrating that densities of charge transfer sites controlled by the number of SLG stacks are important issue for the future production of highly sensitive, uniform SERS substrates comprised of graphene materials.

3. Discussion: Role of graphene thickness in photocatalytic enhancement

We can understand the results described above within work-function diagrams of each GHP shown in Scheme 1. Graphene is the quantized form of graphite crystal along c-axis. Due to the single joint point of valence and conduction bands of graphene at K point, graphene is widely known as a zero band-gap material.[50] Other than the K point, however, electronic band structure of graphene along other vectors exhibits certain gaps, including the direction parallel to c-axis. Stacking of graphene sheets result in discrete energy levels with wave factors normal to graphene surface, observed both experimentally and theoretically in the literature.[51] According to these reported results, the relative energy gaps of 1L, 3L, and 7L graphene stacks can be derived from the measurement of the reflectivity of low-energy electrons from 1 to 7 layer(s) of graphene films. The number of quantized energy levels equals that of stacked graphene sheets, while the work function of each energy levels are determined relative to that of SLG around -4.7 to -4.9 eV (Fig. S-9).[52] Together all the information, the work-function diagram of GHPs can be composed in Scheme 1.

The work-function of graphene is close to the conduction band of anatase TiO_2, facilitating the photoelectron transfer from TiO_2 to SLG.[34] Thus **1L-GHP** exhibits higher photocatalytic efficiency than bare TiO_2. For **3L-GHP**, the gap of energy levels (~2 eV) of 3L graphene is appropriate to accept photoinduced electrons and holes from TiO_2, both active for photocatalysis. Compared to **1L-GHP** that utilizes

7

only photoelectrons for photocatalysis, the much stronger activity of **3L-GHP**, where both photoelectrons and holes are available for photodegradation, can be rationalized. In addition, while photoelectrons continuously transfer to SLG in **1L-GHP**, the holes that accumulate in TiO_2 create a highly positive potential to slow down the photoexcitation process, decreasing the amount of available photoelectrons for photocatalysis. In contrast, the TiO_2 in **3L-GHP** does not accumulate holes resulting in much faster photoexcitation cycles and higher photocatalytic performance.

Although there is no hole accumulation in the TiO_2 of **7L-GHP**, the presence of two additional energy levels with smaller gap (~1 eV) significantly increases the probability of energy relaxation of photoelectrons for falling to the lower energy levels, which is a much faster process than heterogeneous charge transfer at water/O_2/graphene interface. Due to a similar work function between VB of TiO_2 and the lowest energy state of 7L graphene, photoinduced holes can rapidly transfer to 7L graphene stacks. As a consequence, a significant amount of photoinduced charges recombines in the graphene stacks of **7L-GHP** (Scheme 1), where photocatalytic activities and gold deposition are barely enhanced.

With this proposed mechanism, we rationalize the results of oxygen plasma-treated GHPs in which **O-3L-GHP** exhibits the greatest photocatalytic enhancement after the increase of surface hydrophilicity (Fig. 4a and S-6). The higher hydrophilicity in **O-3L-GHP**, compared to pristine **3L-GHP**, results in a better contact of water molecules with graphene surface, which further boosts the charge transfer of photoinduced holes to water yielding oxidative OH· radicals for dye decomposition (Fig. S-8). Due to the lack of hole transfer in **1L-GHP**, the increase of the hydrophilicity in **O-1L-GHP** does not significantly affect its photocatalytic performance. For **O-7L-GHP**, the energy relaxation and recombination processes could still compete effectively with hole transfer at heterogeneous interface of water and graphene. Therefore the effect of plasma oxidization is more pronounced on **O-3L-GHP** than the other two oxidized samples.

Based on the proposed photocatalytically enhancement mechanism, the graphene-enhanced properties should only depend on the number of stacked graphene sheets at the hybrid interface. To verify this mechanism, additional photoactive semiconductor of ZnO, which possesses highly similar work function and identical band gap (3.2 eV) to TiO_2,[13] was used to replace TiO_2 in the original GHPs for photocatalytic tests (Fig. 7). The trend of degradation efficiency observed in ZnO GHPs was identical to that observed in TiO_2 GHPs. The highest and lowest photodegradation rate constants were observed for ZnO **3L-GHP** and **7L-GHP** respectively. Again, the critical thickness of 3L graphene generally enables the maximized photocatalytic enhancement even with different photoactive

semiconductors. These results further support the proposed mechanism above. Graphene thickness is confirmed to be the general key to manipulate graphene-enhanced properties, regardless of the hybridizing species and surface interactions/modifications.

4. Conclusion

We have experimentally demonstrated that graphene thickness is the key determinant that controls the performance of graphene-enhanced photocatalysis, regardless of the hybridized species or graphene surface modification. Three-layer graphene stacks generally manifested the highest activity. Neither the UV transparency nor the surface energy of graphene stacks correlate with the observed photodegradation activity. We propose that the quantized energy levels caused by graphene sheet stacking determine photodegradation activity by altering the kinetics of charge transfer process. The visualization of the presumptive catalytic sites on graphene surface can be achieved by addition of photoelectron scavengers. This concept of direct labelling at graphene/material interfaces can be highly useful for species detection, mechanism studies, interfacial decoration, and preparation of novel nanocomposites. Thus we demonstrated the potential of gold-deposited GHPs as highly SERS-active substrates with the enhancement factors of ~10^8. Our results illustrate the value of the versatile and highly measurement-accessible GHP system as a powerful, general research platform for understanding and exploiting the factors that underlie graphene's capacity to enhance performance in various emerging technologies, especially for clean energy and biomedicine.

5. Experimental

5.1. Preparation of TiO$_2$ and ZnO panels

The TiO$_2$/quartz panels were prepared by the sol-gel method using titanium (IV) oxysulfate as the precursor.[32, 33] An aqueous solution of 0.54 M TiOSO$_4$ was prepared first, followed by an addition of 3 M NH$_4$OH until pH = 12 to yield a white slurry. After stirring for 30 min, the white slurry was filtered and rinsed with deionized water several times. A hydrogen peroxide solution (50 ml, 30%) was mixed with the white slurry and stirred overnight to form a yellow gel. The films of TiO$_2$ on quartz substrates were fabricated by spin-coating (3000 r.p.m. for 30 seconds) using the yellow gel. The films were dried at 60°C for 30 min and calcined at 500°C for 3 hours to produce anatase TiO$_2$ panels.

The ZnO/quartz panels were prepared by sol-gel approach as well using zinc acetate dehydrate as the precursor.[34] A zinc acetate solution (50 mL, 0.04 M) was mixed with NaOH (0.212 M) at 50°C and stirred for 30 min to obtain a white gel. The

white gel was then spun on quartz substrates (3000 r.p.m. for 30 seconds), and dried at $60^{\circ}C$ for 30 min, followed by the calcination at $550^{\circ}C$ for 3 hours to obtain crystalline ZnO panels.

5.2. Fabrication of graphene and graphene hybrid panels (GHPs)

Single layer graphene films were produced on Cu foils by chemical vapor deposition (CVD) under a low pressure condition.[21] Cu foils with desired shapes and dimensions were placed in a quartz tube at 10^{-3} torr. The CVD system was then heated up to $1000^{\circ}C$ with a flow of hydrogen gas (10 sccm) for 20 min to clean and anneal the Cu surface. Subsequently, the atmosphere was changed to a mixture of CH_4 (10 sccm) and H_2 (35 sccm) for 40 min. Finally, the system was cooled to room temperature under argon flow (60 sccm). The graphene produced on the Cu foils was coated with a thin layer of poly (methyl methacrylate) (PMMA, M_w ~996,000) by spin-coating method. The Cu foil was then etched away with an ammonium persulfate solution. The obtained PMMA/graphene layers were transferred to the TiO_2 or ZnO panels and dried for 10 min. The PMMA was dissolved with toluene to produce graphene hybrid panels with one layer of graphene. By repeating the whole transfer procedure 3, 5 and 7 times, GHPs with the 3,5, and 7 graphene layers (**3L-GHP, 5L-GHP, 7L-GHP**) were produced layer-by-layer in addition to a single-layer GHP, **1L-GHP**.

5.3. Oxygen plasma treatment and gold particle photodeposition on GHPs

1L-GHP, **3L-GHP**, and **7L-GHP** were treated by oxygen plasma for 5 seconds with a power of 10 W in a low-pressure oxygen atmosphere (2.1×10^{-1} Torr). The photodeposition of gold particles on the GHP surface was carried out using $HAuCl_4$ solution as the precursor. An ethanol solution (20 mL) of 0.001M $HAuCl_4$ was added in a quartz tube with the selected GHP under the UV irradiation (365 nm, 16W) for 30 min. The products were cleaned with acetone and water.

5.4. Material characterization

The Raman results of CVD graphene were collected by WITec Confocal Raman Microscope using a 532 nm wavelength laser. The values of graphene resistance were measured by a four-point probe station (CHI-5601Y/QT-50). The surface energy measurement was performed using a contact angle goniometer (Sindatek Model 100SB). Scanning electron microscope (SEM) images were acquired with a Zeiss Supra 55 Gemini with an acceleration voltage of 1kV.

5.5. Photocatalytic decomposition and SERS measurement

The photodegradation of organic dyes was monitored using UV-visible spectroscopy (JASCO V-630). Various GHP samples were placed in a quartz tube with 8 mL solutions of methylene blue (2×10^{-4} M) under the irradiation of 365 nm UV light (16 W) in a photoreactor (Photochemical Reactor PR-2000) for 240 minutes. The characteristic absorption band of MB at 665 nm was monitored to study the progress of photodegradation. In the cycle tests of photodegradation, **3L-GHP** was irradiated with 8 mL of MB solutions (1×10^{-4} M) for one hour, repeated for five times. For the SERS experiment, the Raman signals of rhodamine 6G (R6G) was acquired under a 633 nm He-Ne laser with a power of 2 mW. A droplet of R6G solution (in ethanol) with a concentration of 10^{-5} M (and 10^{-3} M for the reference compare substrate) was dropped on the GHP surface and dried under ambient condition. The enhancement factor (EF) of SERS is defined following EF = $(I_{SERS}/I_R)(N_R/N_{SERS})$, where I_{SERS} and I_R are the integrated intensity of R6G peak at 1510 cm^{-1} collected on gold-deposited GHP and reference substrates (TiO$_2$/quartz), respectively; N_{SERS} and N_R are the numbers of molecules gold-deposited GHP and reference substrates, respectively.
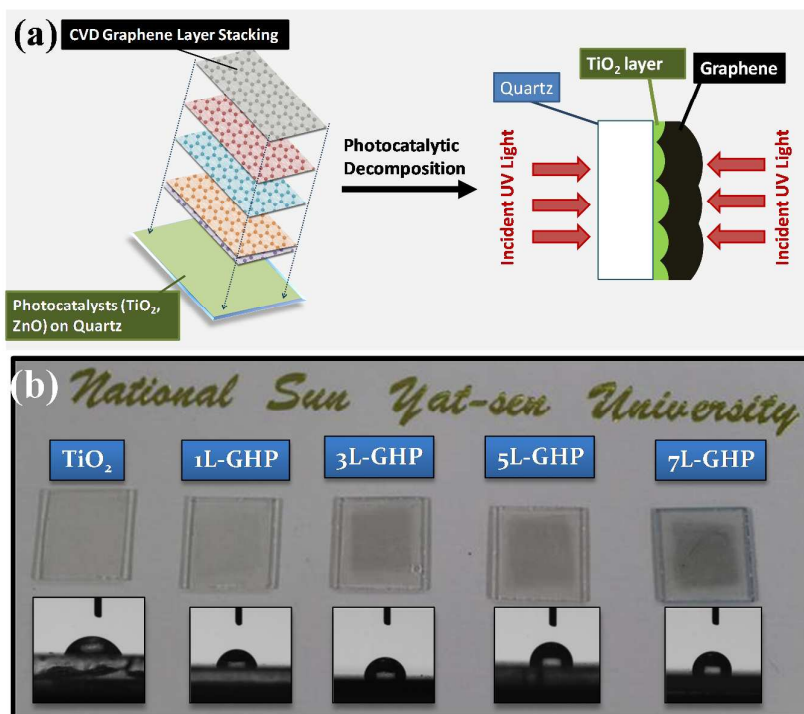
Figure 1. The schematics of the assembly procedure and photographs of GHP substrates. (a) The schematic illustration of GHP assembly for photodegradation. The sandwich-like assembly of GHPs with controlled numbers of individual CVD graphene sheet was supported on photoactive semiconductors/quartz substrates. Keeping GHPs vertical in photodegradation tests maximized UV flux. (b) The photographs and contact angles (insets) of GHP substrates. Both the graphene contrast and contact angles increase with the number of the stacked graphene sheets.
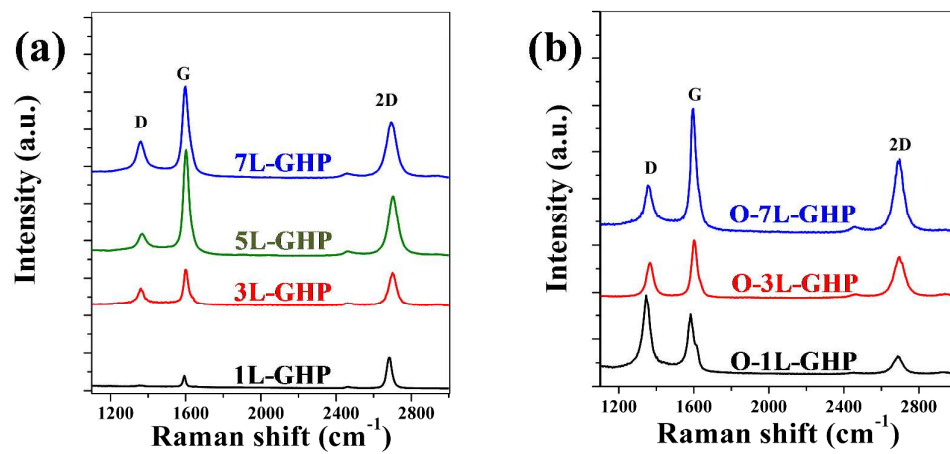
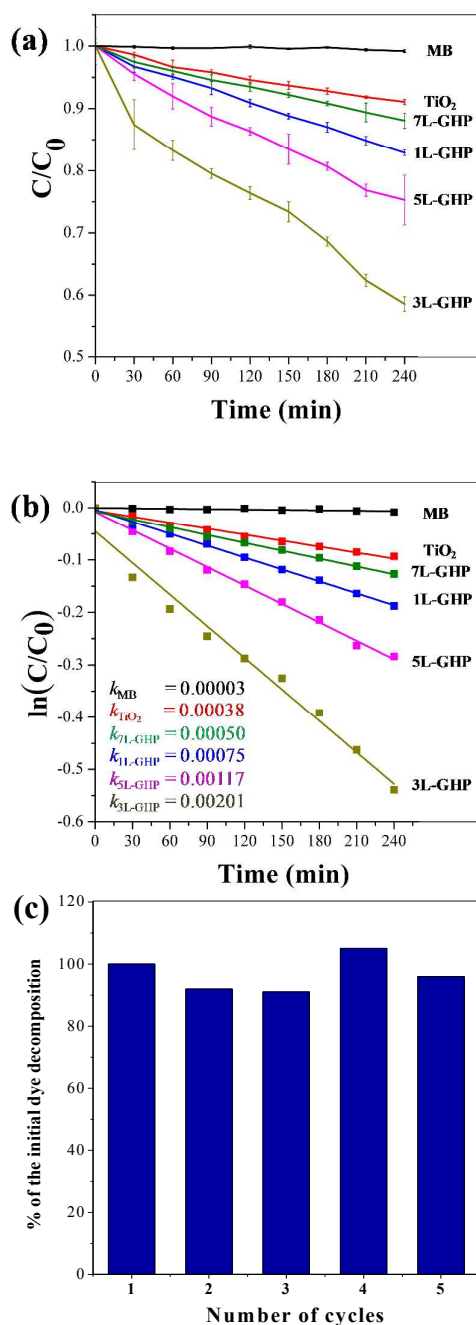Figure 2. The Raman spectra of (a) as prepared and (b) oxygen-plasma treated GHP samples.

Figure 3. The concentration of methylene blue (MB) in contact with TiO_2 and GHP substrates as the function of irradiation time (a). Lines in (b) are least-squares fits giving the listed pseudo-first order rate constants based on the results in (a). (c) The cycle tests of photodegradation of **3L-GHP**. One particular **3L-GHP** sample was tested repeatedly for photodegradation of MB for five cycles. The amounts of photodecomposed MB in each cycle were compared to that of the first cycle and expressed in percentage.
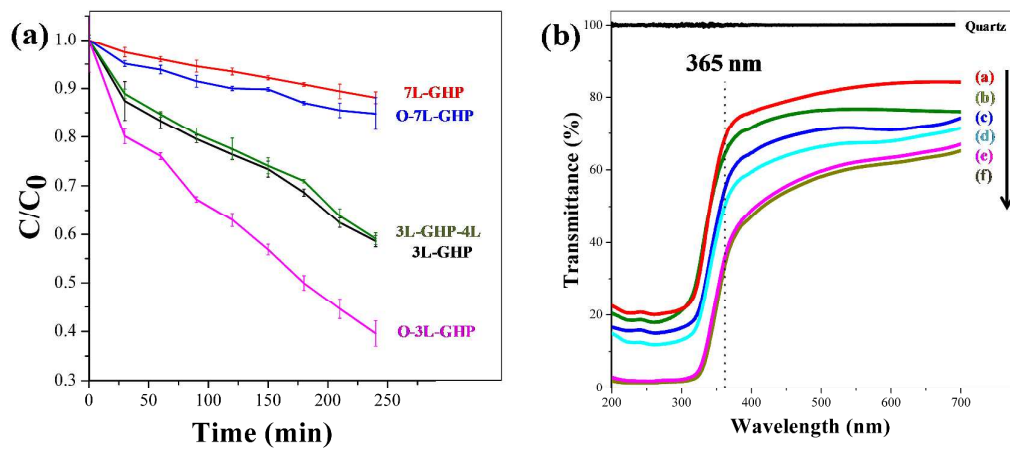
14

Figure 4. (a) Comparison of changes in the concentration of MB in solutions in contact with the oxygen plasma treated samples (**O-3L-GHP** and **O-7L-GHP**) and the untreated ones (**3L-GHP**, **7L-GHP**, and **3L-GHP-4L**) as a function of irradiation time. (b) The transmittance results of GHPs. From (a) to (f) are results for bare TiO_2, **1L-GHP**, **3L-GHP**, **5L-GHP**, **3L-GHP-4L**, and **7L-GHP**, respectively.
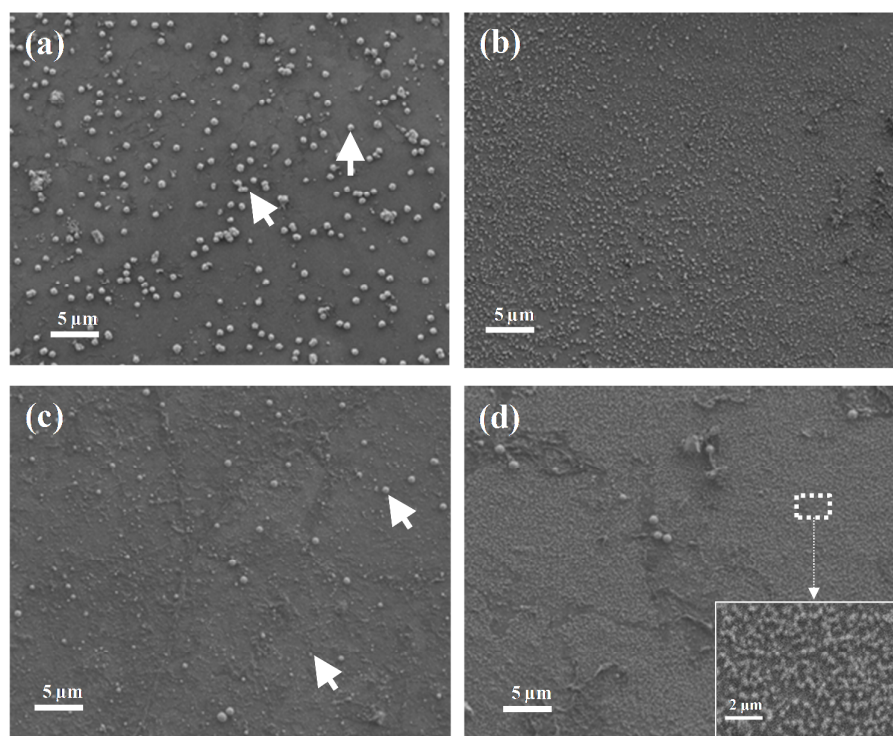
Figure 5. The SEM images of GHPs with gold particles deposited on the graphene surface under the UV irradiation for 30 min: (a) **1L-GHP**, (b) **3L-GHP**, (c) **7L-GHP**, and (d) **O-3L-GHP**. All the images were taken with the same magnification. The white dash-line square area in (d) corresponds to the inset image. In (a) and (c), white arrows identify gold particles with the relatively large diameters of 500-700 nm. For (b) and (d), the fine gold particles were fairly uniform and covered the whole surface. The particle diameters in (b) and (d) are 150-200 nm and 80-100 nm, respectively.
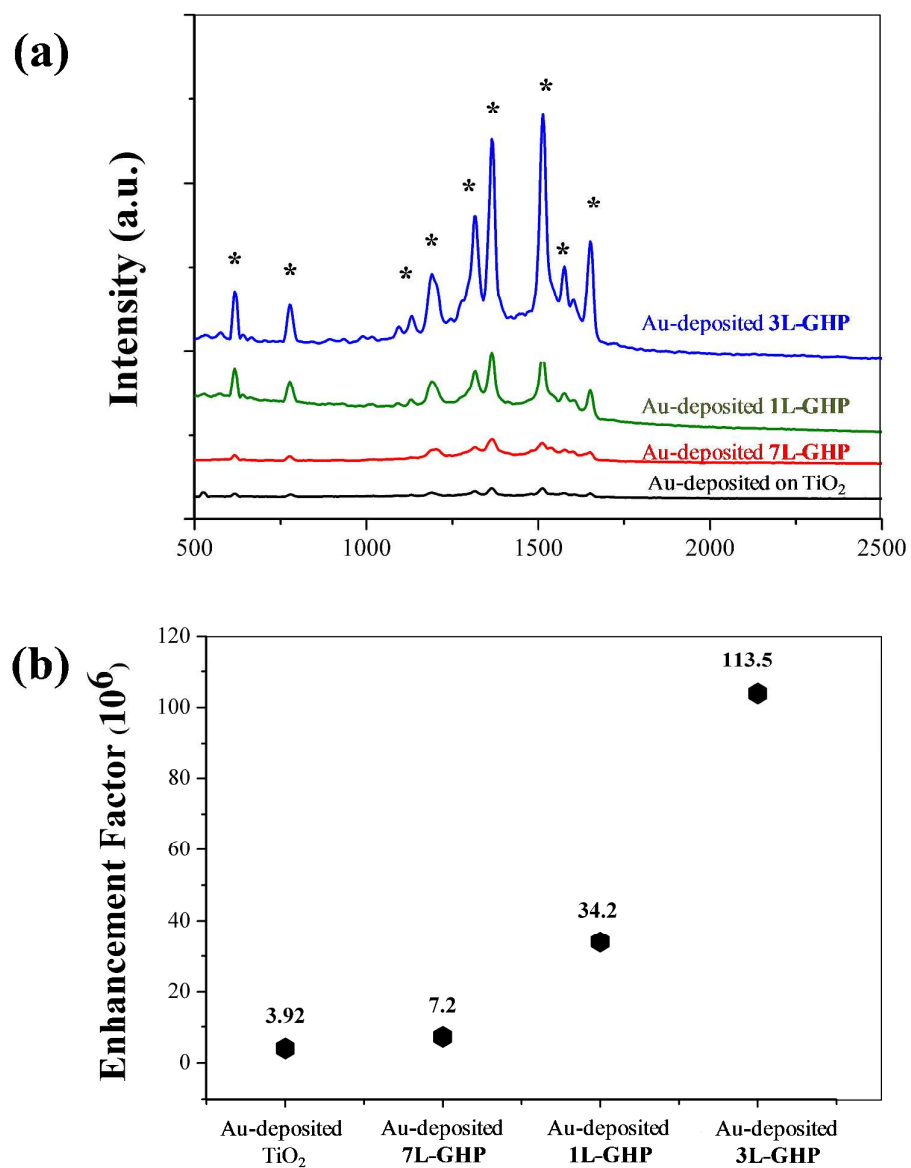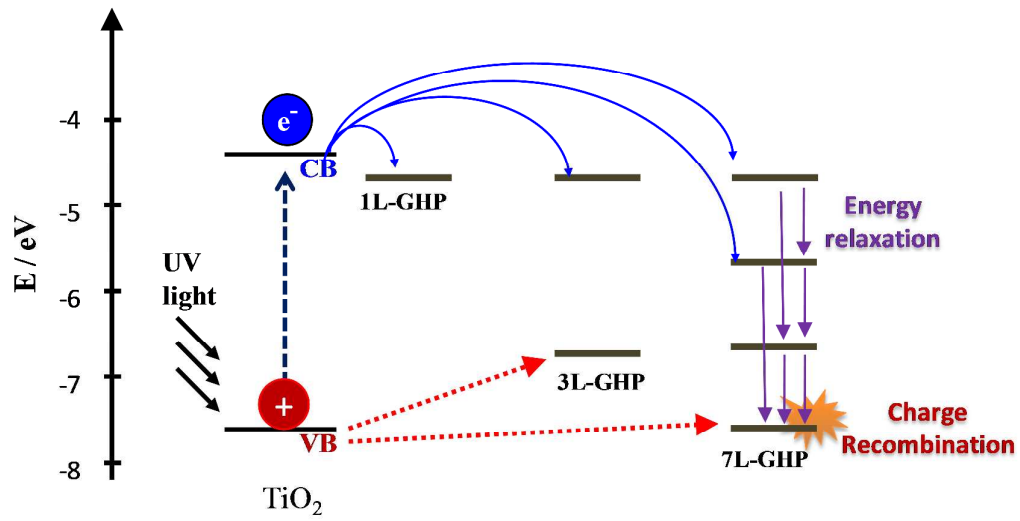
(a)

(b)

Figure 6. The SERS signals of R6G in the presence of gold-deposited GHPs with different graphene thickness. The peaks labelled with star correspond to the vibration modes of R6G. (b) The comparison of enhancement factors obtained in (a).

Scheme 1. The schematics of the proposed charge transfer processes for bare TiO_2 and GHPs with different number of graphene layers. In **3L-GHP** and **7L-GHP**, the energy levels higher than TiO_2 conduction band are not shown.
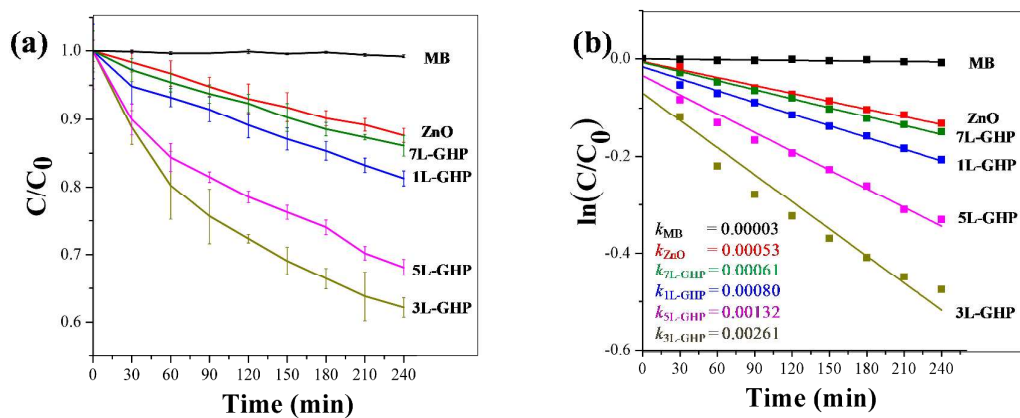
Figure 7. The photodegradation efficiency of methylene blue (MB) with ZnO GHP substrates as the function of reaction time. (a) The concentration changes of MB during the incubation with various ZnO GHPs under the UV-light irradiation. (b) The MB photodegradation efficiency obtained in (a) is presented by pseudo-first order fitting with the corresponding rate constants.

Table 1. The summary of resistance and contact angles of TiO_2 GHPs.

Samples	Resistance (Ω/square)	Contact angles (degree)
TiO_2	N.A.	71.8 ± 6.0
1L-GHP	201	78.9 ± 6.5
3L-GHP	135	96.5 ± 2.7
5L-GHP	99	100.5 ± 5.4
7L-GHP	82	101.9 ± 6.0
O-1L-GHP	9325	50.6 ± 5.6
O-3L-GHP	801	71.0 ± 8.5
O-7L-GHP	695	98.0 ± 5.2

Reference

1.   K. S. Novoselov, A. K. Geim, S. V. Morozov, D. Jiang, Y. Zhang, S. V. Dubonos, I. V. Grigorieva and A. A. Firsov, *Science*, 2004, **306**, 666-669.
2.   C. Lee, X. Wei, J. W. Kysar and J. Hone, *Science*, 2008, **321**, 385-388.
3.   L. G. D. Arco, C. Zhou, Y. Zhang, C. W. Schlenker, K. Ryu and M. E. Thompson, *ACS Nano*, 2010, **5**, 2865-2873.
4.   D. Wang, D. Choi, J. Li, Z. Yang, Z. Nie, R. Kou, D. Hu, C. Wang, L. V. Saraf, J. Zhang, I. A. Aksay and J. Liu, *ACS Nano*, 2009, **3**, 907-914.
5.   Y. Liang, Y. Li, H. Wang, J. Zhou, J. Wang, T. Regier and H. Dai, *Nat. Mater.*, 2011, **10**, 780-786.
6.   K. Parvez, S. Yang, Y. Hernandez, A. Winter, A. Turchanin, X. Feng and K. Mullen, *ACS Nano*, 2012, **11**, 9541-9550.
7.   D. I. Son, C.-L. Lee, B. Kwon, W. K. Choi, D. Park, W.-S. Seo, Y. Yi and B. Angadi, *Nat. Nanotechnol.*, 2012, **7**, 465-471.
8.   J. H. Jung, D. S. Cheon, F. Liu, K. B. Lee and T. S. Seo, *Angew. Chem., Int. Ed.*, 2010, **49**, 5708-5711.
9.   X. Huang, Z. Zeng, Z. Fan, J. Liu and H. Zhang, *Adv Mater*, 2012, **24**, 5979-6004.
10. B. Qiu, M. Xing and J. Zhang, *J. Am. Chem. Soc.*, 2014, **136**, 5852-5855.
11. H. Zhou, C. Qiu, Z. Liu, H. Yang, L. Hu, J. Liu, H. Yang, C. Gu and L. Sun, *J. Am. Chem. Soc.*, 2009, **132**, 944-946.
12. J. Rafiee, X. Mi, H. Gullapalli, A. V. Thomas, F. Yavari, Y. Shi, P. M. Ajayan and N. A. Koratkar, *Nat. Mater.*, 2012, **11**, 217-222.
13. A. L. Linsebigler, G. Lu and J. T. Yates, *Chem. Rev.*, 1995, **95**, 735-758.
14. M. G. Walter, E. L. Warren, J. R. McKone, S. W. Boettcher, Q. Mi, E. A. Santori and N. S. Lewis, *Chem. Rev.*, 2010, **110**, 6446-6473.
15. I. K. Konstantinou and T. A. Albanis, *Appl. Catal., B*, 2004, **49**, 1-14.
16. L. Xu, Y.-L. Hu, C. Pelligra, C.-H. Chen, L. Jin, H. Huang, S. Sithambaram, M. Aindow, R. Joesten and S. L. Suib, *Chem. Mater.*, 2009, **21**, 2875-2885.
17. Q. Xiang, J. Yu and M. Jaroniec, *Chem. Soc. Rev.*, 2012, **41**, 782-796.
18. T. Xu, L. Zhang, H. Cheng and Y. Zhu, *Appl. Catal., B*, 2011, **101**, 382-387.
19. G. Williams, B. Seger and P. V. Kamat, *ACS Nano*, 2008, **2**, 1487-1491.
20. J. S. Lee, K. H. You and C. B. Park, *Adv. Mater.*, 2012, **24**, 1084-1088.
21. M. S. Sher Shah, A. R. Park, K. Zhang, J. H. Park and P. J. Yoo, *ACS Appl. Mater. Interfaces*, 2012, **4**, 3893-3901.
22. H. Zhang, X. Lv, Y. Li, Y. Wang and J. Li, *ACS Nano*, 2009, **4**, 380-386.
23. O. Akhavan and E. Ghaderi, *J. Phys. Chem. C*, 2009, **113**, 20214-20220.
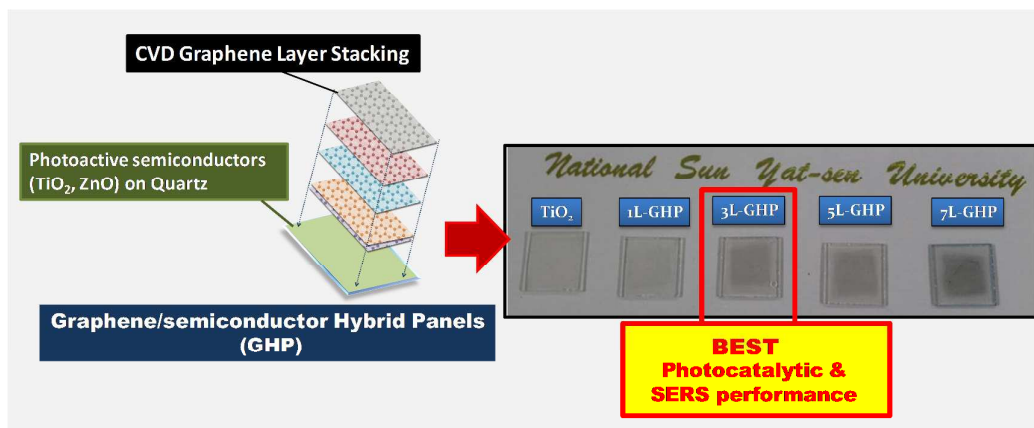
Nanoscale Accepted Manuscript

24.   Y. T. Liang, B. K. Vijayan, K. A. Gray and M. C. Hersam, *Nano Lett.*, 2011, **11**, 2865-2870.

25.   M. Xing, X. Li and J. Zhang, *Sci. Rep.*, 2014, **4**, 5493.

26.   W. S. Hummers and R. E. Offeman, *J. Am. Chem. Soc.*, 1958, **80**, 1339-1339.

27.   X. Li, W. Cai, J. An, S. Kim, J. Nah, D. Yang, R. Piner, A. Velamakanni, I. Jung, E. Tutuc, S. K. Banerjee, L. Colombo and R. S. Ruoff, *Science*, 2009, **324**, 1312-1314.

28.   S. Lee, K. Lee and Z. Zhong, *Nano Lett.*, 2010, **10**, 4702-4707.

29.   A. C. Ferrari, J. C. Meyer, V. Scardaci, C. Casiraghi, M. Lazzeri, F. Mauri, S. Piscanec, D. Jiang, K. S. Novoselov, S. Roth and A. K. Geim, *Phys. Rev. Lett.*, 2006, **97**, 187401.

30.   H. Kim, I. Song, C. Park, M. Son, M. Hong, Y. Kim, J. S. Kim, H.-J. Shin, J. Baik and H. C. Choi, *ACS Nano*, 2013, **8**, 6575-6582.

31.   L. Jiang, T. Niu, X. Lu, H. Dong, W. Chen, Y. Liu, W. Hu and D. Zhu, *J. Am. Chem. Soc.*, 2013, **135**, 9050-9054.

32.   Z. Yan, Z. Peng, Z. Sun, J. Yao, Y. Zhu, Z. Liu, P. M. Ajayan and J. M. Tour, *ACS Nano*, 2011, **10**, 8187-8192.

33.   J. Zhao, T. Wu, K. Wu, K. Oikawa, H. Hidaka and N. Serpone, *Environ. Sci. Technol.*, 1998, **32**, 2394-2400.

34.   S. Liu, C. Liu, W. Wang, B. Cheng and J. Yu, *Nanoscale*, 2012, **4**, 3193-3200.

35.   X. Chen, G. Zhou, X. Peng and J. Yoon, *Chem. Soc. Rev.*, 2012, **41**, 4610-4630.

36.   J. Lee, H. Jun and J. Kim, *Adv. Mater.*, 2009, **21**, 3674-3677.

37.   S. Kim, S. H. Ku, S. Y. Lim, J. H. Kim and C. B. Park, *Adv. Mater.*, 2011, **23**, 2009-2014.

38.   I. Ilisz, Z. Laszlo and A. Dombi, *Appl. Catal. A*, 1999, **180**, 25-33.

39.   R. Long, N. J. English and O. V. Prezhdo, *J. Am. Chem. Soc.*, 2012, **134**, 14238-14248.

40.   M. Niu, D. Cheng and D. Cao, *J. Phys. Chem. C*, 2014, **118**, 5954-5960.

41.   M. Niu, D. Cheng and D. Cao, *Sci. Rep.*, 2014, **4**, 4810.

42.   Z. Fan, R. Kanchanapally and P. C. Ray, *J. Phys. Chem. Lett.*, 2013, **4**, 3813-3818.

43.   X. Ling, L. Xie, Y. Fang, H. Xu, H. Zhang, J. Kong, M. S. Dresselhaus, J. Zhang and Z. Liu, *Nano Lett.*, 2010, **10**, 553-561.

44.   E. S. Thrall, A. C. Crowther, Z. Yu and L. E. Brus, *Nano Lett.*, 2012, **12**, 1571-1577.

45.   C. Marichy, M. Bechelany and N. Pinna, *Adv. Mater.*, 2012, **24**, 1017-1032.

46.   X. Wang, M. Li, L. Meng, K. Lin, J. Feng, T. Huang, Zhilin Yang and B. Ren, *ACS Nano*, 2014, **8**, 528-536.

Nanoscale Accepted Manuscript

47.   D. Qi, L. Lu, L. Wang and J. Zhang, *J. Am. Chem. Soc.*, 2014, **136**, 9886-9889.

48.   Q. Su, X. Ma, J. Dong, C. Jiang and W. Qian, *ACS Appl. Mater. Interfaces*, 2011, **3**, 1873-1879.

49.   F. D. Mai, T. C. Hsu, Y. C. Liu, K. H. Yang and B. C. Chen, *Chem. Commun.*, 2011, **47**, 2958-2960.

50.   R. Mas-Balleste, C. Gomez-Navarro, J. Gomez-Herrero and F. Zamora, *Nanoscale*, 2011, **3**, 20-30.

51.   H. Hibino, H. Kageshima, F. Maeda, M. Nagase, Y. Kobayashi and H. Yamaguchi, *Phys. Rev. B*, 2008, **77**, 075413-075411.

52.   D. Zhang, L. Gan, Y. Cao, Q. Wang, L. Qi and X. Guo, *Adv. Mater.*, 2012, **24**, 2715-2720.

Acknowledgement

Nanoscale Accepted Manuscript

Table of contents

Graphene thickness is the key determinant that controls the performance of graphene-enhanced photocatalysis and SERS applications.